Pervasive Transcriptome Interactions of Protein-Targeted Drugs

Linglan Fang, Willem A. Velema, Yujeong Lee, Xiao Lu, Michael G. Mohsen, Anna M. Kietrys, and Eric T. Kool*
Department of Chemistry and Sarafan ChEM-H Institute, Stanford University, Stanford, CA 94305
*Author to whom correspondence should be addressed: kool@stanford.edu

The off-target toxicity of drugs targeted to proteins imparts substantial health and economic costs. Proteome interaction studies can reveal off-target effects with unintended proteins; however, little attention has been paid to intracellular RNAs as potential off targets that may contribute to toxicity. To begin to assess this, we developed a reactivity-based RNA profiling (RBRP) methodology, and applied it to uncover transcriptome interactions of a set of FDA-approved small-molecule drugs *in vivo*. We show that these protein-targeted drugs pervasively interact with the human transcriptome and can exert unintended biological effects on RNA function. In addition, we show that many off-target interactions occur at RNA loci associated with protein binding and structural changes, allowing us to generate hypotheses to infer the biological consequences of RNA off-target binding. The results suggest that rigorous characterization of drugs' transcriptome interactions may help assess target specificity and avoid toxicity and clinical failures.

Dose-limiting toxicity is a routinely encountered problem in therapeutic drug development that is often discovered in clinical trials[1]. This is both detrimental to positive human health outcomes and costly in capital and human effort. Even for approved drugs, dose-limiting toxicity results in adverse outcomes and post-marketing drug withdrawal[2]. These drug toxicities are commonly attributed to off-target binding to unintended cellular proteins[3]. Given RNA's broad bioregulatory roles in human physiology and the structural resemblance of protein-targeted drugs with known RNA-binding molecules[4,5] (**Fig. 1a-c**), we hypothesize that many protein-targeted small-molecule drugs can interact with the human transcriptome (and RNA-protein interfaces) and may confer serious toxicity in patients. Indeed, our analysis suggests that nearly 35% of all small-molecule FDA-approved drugs chemically resemble at least one known RNA-binding molecule (Tanimoto coefficient[6] ≥0.7) (**Fig. 1a-b** and **Supplementary file S1**), and at least ten approved drugs are already documented as RNA binders *in vitro* (**Supplementary file S2**)[4,5]. Such chemical similarity with RNA-binding molecules also extends to drugs from preclinical studies and all phases in clinical trials (**Fig. 1c**).

Little is known about the RNA off-target interactions of protein-targeted drugs *in vivo*, especially for clinically approved drugs. Investigation of small molecule-RNA interactions has been carried out recently via photocrosslinking (diazirine)[7,8], alkylation (chlorambucil)[9,10], in-line probing[11], and SHAPE[12], and these have emerged as useful tools to identify RNA-ligand interactions *in vitro* and recently in cultured cells[13]. Although elegant, application of these methods *in vivo* is potentially limited by transcriptional effects during prolonged probe treatment[14], cellular damage by ultraviolet irradiation[15,16], and nucleobase biases[17-19]. We address these challenges by developing cell-permeable RNA 2′-hydroxyl (2′-OH) acylating analogs of drugs that permit *in vivo* analysis of RNA-drug contacts in a sequence-independent manner. This reactivity-based RNA profiling (RBRP) methodology allows us to decode transcriptome interactions of drugs via deep sequencing and bioinformatics (**Fig. 1d**).

In this study, we employed RBRP to map *in vivo* transcriptome interactions of representative protein-targeted drugs in human cells. We provide first-in-class evidence that RNA off-targets exist for FDA-approved protein-targeted drugs in cells. These transcriptome interactions are largely determined by the chemical structure of small-molecule drugs. We further demonstrate that drug engagement with RNA off-targets can exhibit target-associated cellular outcomes; for example, drug engagement with snoRNA sequences modulates downstream 2′-OH methylation of ribosomal RNAs. Moreover, RBRP enables mapping of the binding site across ~16,000 RNAs containing a poly(A) tail with nucleotide-level precision, and reveals intricate interplay of RNA-drug binding, RNA-binding proteins (RBP), and RNA structural accessibility and dynamics.

Results and discussion

RBRP decodes transcriptome interactions of protein-targeted small-molecule drugs *in vivo*. Our profiling methodology involves the use of cell-permeable RNA acylation probes (employing acylimidazole-substituted linkers to react at RNA 2′-OH groups) to evaluate and quantify the tendency of drugs to bind cellular RNAs (**Fig. 1d**). The binding of an acylimidazole conjugate of a drug to a structured RNA or protein-RNA interface should lead to enrichment of acylated 2′-OH near the drug binding sites. We identify this binding-promoted acylation by modifying *in vivo* RNA mapping protocols[20], analyzing messenger RNAs (mRNAs) and noncoding RNAs (ncRNAs) by poly(A) pulldown and deep sequencing the resulting libraries at high depth (>11 million reads per replicate). Specifically, RNA drug-binding sites are enriched with acylated 2′-OH groups, which cause reverse transcriptase (RT) to stop. These stops are enriched over random RNA breaks and random site reactions by biotin-mediated pulldown[20] and by competition with the unmodified drug. This comparative workflow allows us to pinpoint and quantify precise binding locations within the entire cellular RNA population; only sites that exhibit competition with the unmodified drug are scored as authentic drug-binding sites.

RBRP reveals the transcriptome interactions of hydroxychloroquine (HCQ). As an initial assessment of *in vivo* transcriptome-interaction of a small molecule drug, we prototyped RBRP experiments with an acylimidazole conjugate of the drug hydroxychloroquine (HCQ), containing an azido "click" handle, in human embryonic kidney cells HEK293 (**Fig. 2a-b**). HCQ, originally approved for the treatment of malaria and recently studied for treatment of COVID-19 infections, is known to cause retinopathy and cardiomyopathy of unknown origins[21,22]. Its structure suggests possible affinity for folded RNAs, given its fused aromatic rings and positive charge, as well as its close structural similarity with known RNA binders (**Fig. 2a**, right panel). To test this possibility, we treated HEK293 cells with the acylating analog of HCQ (HCQ-AI, **Fig. 2b**) for 30 minutes in the absence or presence of excess competing drug (unmodified HCQ), and performed RBRP for poly(A)+ transcripts. We used the icSHAPE pipeline[20,23] (read depth= 200 as threshold) to

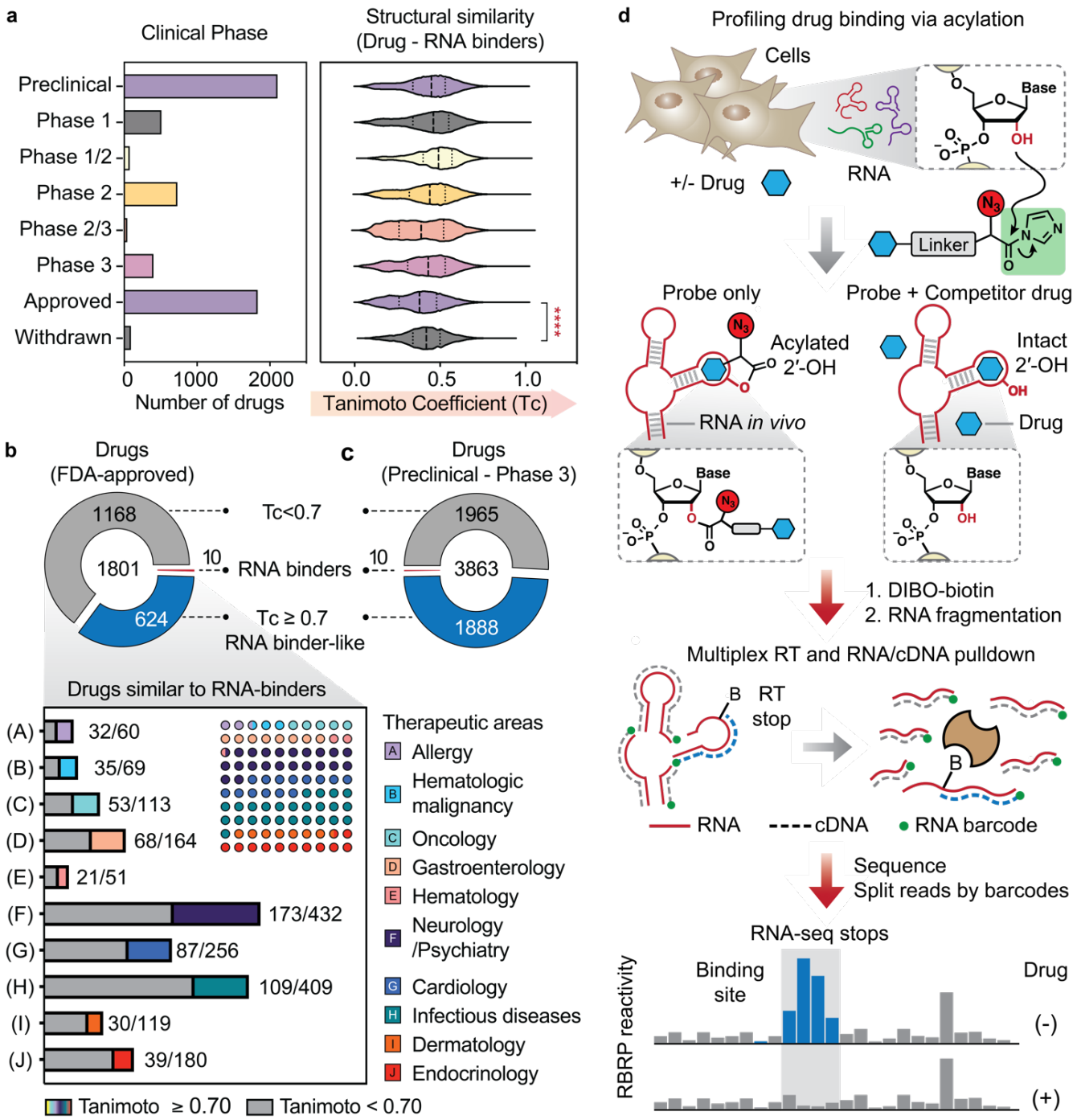

Fig. 1 | RBRP decodes transcriptome-interaction of protein-targeted small-molecule drugs *in vivo*. a, Structure key-based 2D Tanimoto coefficient (Tc) characterizes pairwise structural similarity between 131 reported small-molecule RNA binders[5] and 6043 drugs at various clinical phases. Number of small-molecule drugs at each clinical phase[24] (left panel). **b**, Fractions of FDA-approved drugs that structurally resemble at least one known RNA binder in the top 10 therapeutic areas. **c**, Fractions of drugs from preclinical to phase 3 stages that structurally resemble at least one known RNA binder as measured by Tanimoto coefficient. See **Supplementary file S1** for data. **d**, Schemes for comparative Reactivity-Based RNA Profiling (RBRP) to identify transcriptome-interaction of small-molecule drugs. Acylating analog of drug binds rapidly at specific RNA sites, promoting local acylation, which is analyzed by reverse transcription (RT) stops via multiplexed RNA sequencing (RNA-Seq). Pulldown of acylated RNAs greatly enhances signal/noise, and competition with unmodified drugs reveals specific sites. Binding sites exhibit statistically significant differences in RBRP reactivities.

calculate the frequencies of RT stops as RBRP reactivities to measure probe-promoted 2′-OH acylation and generated 0.8 billion measurements *in vivo*. Enrichment scores were calculated as the ratio of relative RBRP scores (average RBRP score of a 100 nucleotide (nt)-window covering the competed acylation sites) for experiments performed in the absence over the presence of excess competing drug. To stringently eliminate the low-confidence transcriptome interactions, we defined significant RNA off targets as nucleotides with enrichment scores ≥3 and *P*-values <0.05.

These comparative RBRP data allowed us to identify probe-promoted, HCQ-competable 2′-OH acylations as imprints of selective RNA-ligand interactions. Approximately four selective targets were identified in ~16,000 RNAs of HEK293 cells.

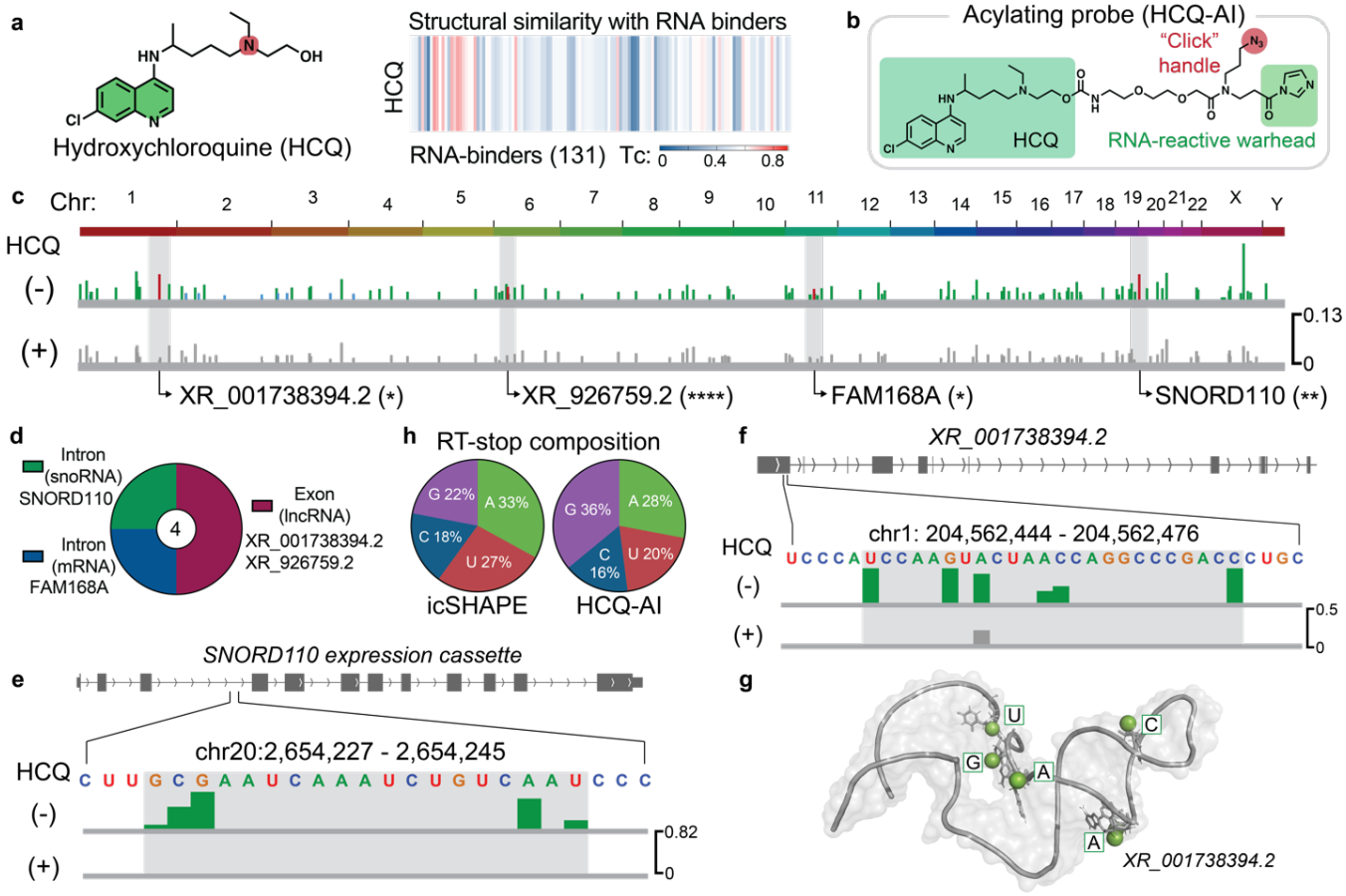

Fig. 2 | RBRP reveals transcriptome-interaction of hydroxychloroquine (HCQ). a, Pervasive structural similarity between the hydroxychloroquine (HCQ) and 131 RNA binders. Heatmap showing the pairwise 2D Tanimoto coefficient (Tc) between HCQ and RNA binders (right panel). Fused aromatic rings are colored in green. Positive charge is colored in red. **b**, A modular design of acylating probe to identify transcriptome-interaction of small-molecule drugs. **c**, UCSC tracks showing RBRP reactivity scores (y-axis) in live HEK293 cells along the human chromosomes in the absence (*top*) or presence (*bottom*) of unmodified HCQ. RBRP reactivity scores are scaled from 0 (no reactivity) to 1 (maximum reactivity). **d**, Donut chart showing target distributions of different RNA types. **e-f**, RBRP data tracks showing HCQ-AI targets SNORD110 expression cassette (**e**) and XR_001738394.2 (**f**) *in vivo*. **g**, Location of probe-acylated 2′-OH (green sphere) mapped onto the 3D model of XR_001738394.2. The three-dimensional RNA structure was modeled using RNAComposer with icSHAPE data[25]. **h**, Comparing reverse transcription (RT) stop distribution transcriptome wide. Structural profiling (icSHAPE) was performed with the benchmark acylimidazole NAI-N_3[20], and RBRP was performed with HCQ-AI.

Several of these were independently confirmed by RT-qPCR (**Supplementary Fig. S1** and **file S3**). We found that RNA off-targets of HCQ were enriched for introns of pre-mRNA and lncRNAs (**Fig.2c-d**). For example, HCQ engaged with the expression cassette of a small nucleolar RNA (SNORD110) at the intron of NOP56 pre-mRNA (**Fig. 2e**). RBRP also provided information about drug-binding sites at near single-nucleotide level; for example, HCQ targeted a highly structured region of the lncRNA XR_001738394.2 (**Fig. 2f-g**). Notably, the nucleotide composition in the RBRP libraries is distributed almost evenly across all four nucleobases, with a slight enrichment for guanosine (**Fig. 2h**). This is in contrast with recent *in vitro* profiling methods that display pronounced biases toward purine nucleobases, especially guanine[17-19]. Moreover, HCQ-AI causes distinct RT stop patterns when compared to the structural profiling reagent (NAI-N_3) used in icSHAPE[20,23,25], strongly suggesting that RBRP signals are promoted by specific drug binding and do not merely reflect the accessibility of 2′-OH groups. Taken together, the data establish the viability of RBRP for profiling ligand-RNA interactions, and identify several specific transcripts and sites of HCQ binding.

Structural fingerprints of small-molecule drugs determine their transcriptome interactions *in vivo*. Existing protein-targeted drugs differ greatly in their physicochemical and molecular recognition features, covering a broad multidimensional chemical space (**Fig. 3a** and **Supplementary Table S1-2**). To explore the generality of transcriptome-interaction of protein-targeted drugs, we next explored two compounds that are structurally distinct from HCQ and that have strongly divergent protein targets. Thus, we characterized the *in vivo* transcriptome-interaction of Levofloxacin (Lev), a member of widely prescribed fluoroquinolone antibiotics known to cause neuropathy, fatigue, and depression in patients[26], and Dasatinib (Das), a multi-targeted kinase inhibitor known to causes neutropenia and myelosuppression, heart failure, and serious pulmonary arterial hypertension[27]. Linkers containing an acylimidazole RNA-reactive warhead and an azide handle were installed in both compounds (**Fig. 3b**).

Profiling of these new compounds via RBRP revealed distinct off-target interactions of Lev and Das with the human transcriptome in cells (**Fig. 3c-d**), consistent with two drugs that differ greatly in their structural fingerprints related to H-bonding,

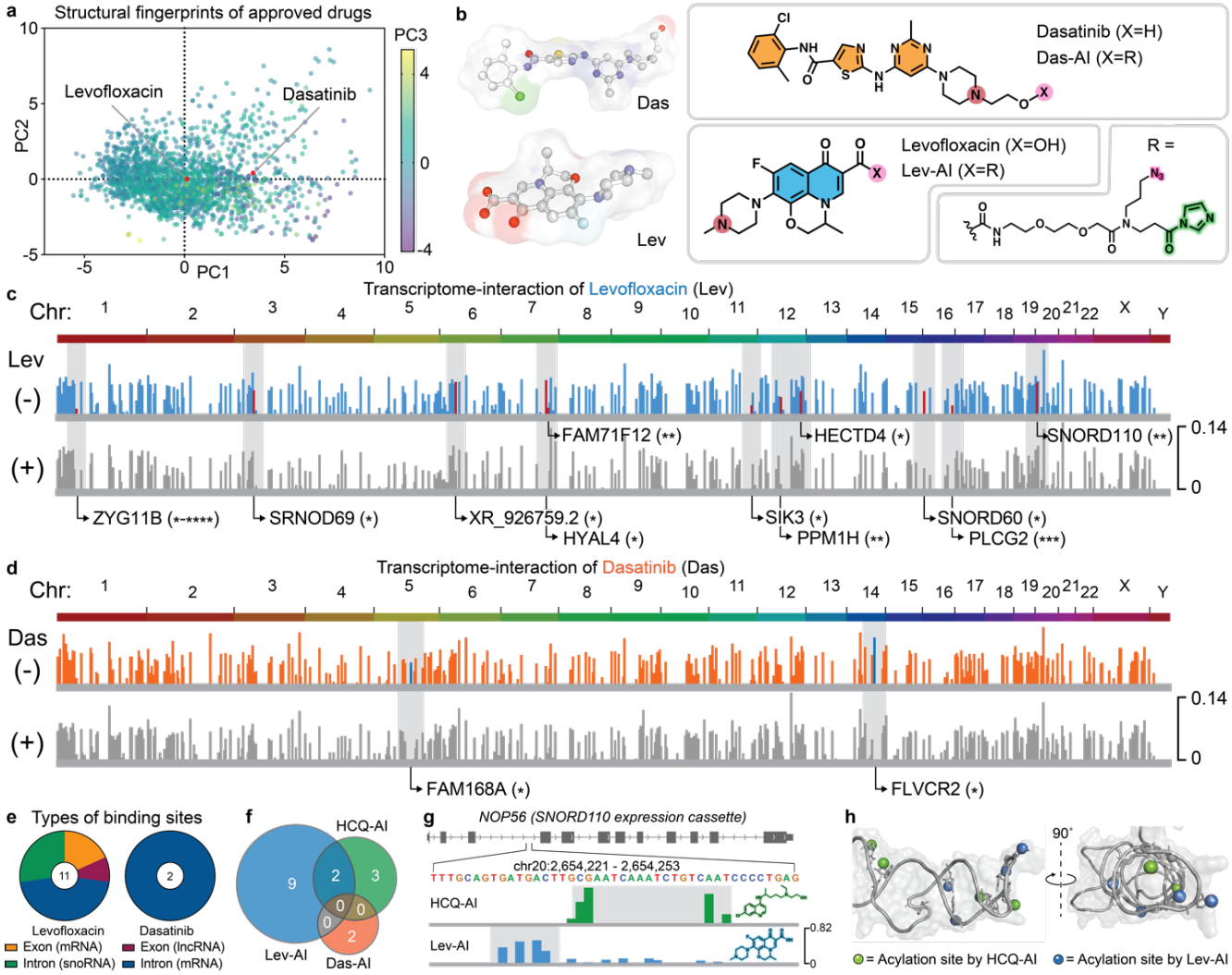

Fig. 3 | Structural fingerprints of small-molecule drugs determine their transcriptome interactions *in vivo*. **a**, Principal component analysis (PCA) describing the variance within the selected FDA-approved drug library. Multivariate plot showing PC1, PC2, and PC3. ChemMineTools calculate the Open Babel descriptors as structural fingerprints[28]. Contributions of each parameter and the loading plots for the first three principal components are shown in SI Fig.Sx. **b**, Chemical structures of Levofloxacin, Dasatinib, and their corresponding acylating probes (Lev-AI and Das-AI). **c-d**, Transcriptome-wide UCSC tracks of RT stops by Lev-AI (**c**) and Das-AI (**d**) in the presence or absence of excessive Levofloxacin (**c**) and Dasatinib (**d**). RBRP reactivity scores are scaled from 0 (no reactivity) to 1 (maximum reactivity). Competed probe binding sites are highlighted as red (**c**) and blue (**d**) bars in grey boxes. Statistical significance was calculated with one-tailed Student's t-tests using the average RBRP reactivities within regions enriched with RT-stops (shown in **Supplementary file S3**): **P*<0.05, ***P*<0.01, ****P*<0.001, *****P*<0.0001. **e**, Donut charts showing the binding site distribution of different RNA types. **f**, Venn diagram for shared *in vivo* RNA targets of HCQ-AI, Lev-AI, and Das-AI. **g**, SNORD110 expression cassette in NOP56 pre-mRNA is a shared target for HCQ-AI and Lev-AI. **h**, HCQ-AI and Lev-AI acylate distinct 2′-OH groups of SNORD110 expression cassette. The location of probe-acylated 2′-OH (HCQ-AI: green; Lev-AI: blue) mapped onto the 3D model of SNORD110 expression cassette. RNA structure was modeled using RNAComposer with icSHAPE data[25].

molecular volume, and London dispersive forces that govern their drug-receptor interactions (**Supplementary Table S3**). Of the two, Lev structurally more closely resembles known RNA binders (**Supplementary Fig. S2**), with an intercalator-like structure incorporating fused heterocycles and cationic charge that likely contribute to its RNA affinity. We identified a range of transcriptome interactions of Lev with at least 12 highly structured RNA loci (**Fig. 3c** and **Supplementary Fig. S3**). The cationic Das also contains heterocyclic flat structures, and amide linkages, reminiscent of groove-binding ligands for nucleic acids[29,30]. Base stacking and partial intercalation by Das are also likely feasible. However, the transcriptome interactions of Das were found to be fewer in number than either Lev or HCQ (**Fig. 3d-e**). In general, all three drugs studied here show a preference for targeting intronic RNA sequences (**Fig. 3e**), consistent with introns constituting up to 35% of the human genome and exons only covering ~2.8% of the genome[31]. As introns play myriad roles in cellular biology (e.g., transcription regulation, alternative splicing, and expressing non-coding RNAs)[32-34], unintended effects on these cellular functions seem quite possible.

The structural fingerprints of small-molecule drugs not only affect their RNA engagement *in vivo*, but also likely the drug binding pose at each RNA off-target site. HCQ and Lev share similar quinoline and quinolone scaffolds, and both drugs target two cellular RNAs in common, including an intronic sequence that expresses snoRNA (SNORD110) and a lncRNA (XR_926759.2 or RNU1-88P) (**Fig. 3f**). Notably, we found that both of these drugs bind to the substrate recognition sequence of the SNORD110 (**Fig. 3g**), albeit at different subsites on this RNA. RBRP revealed distinct acylation patterns by HCQ-AI and Lev-

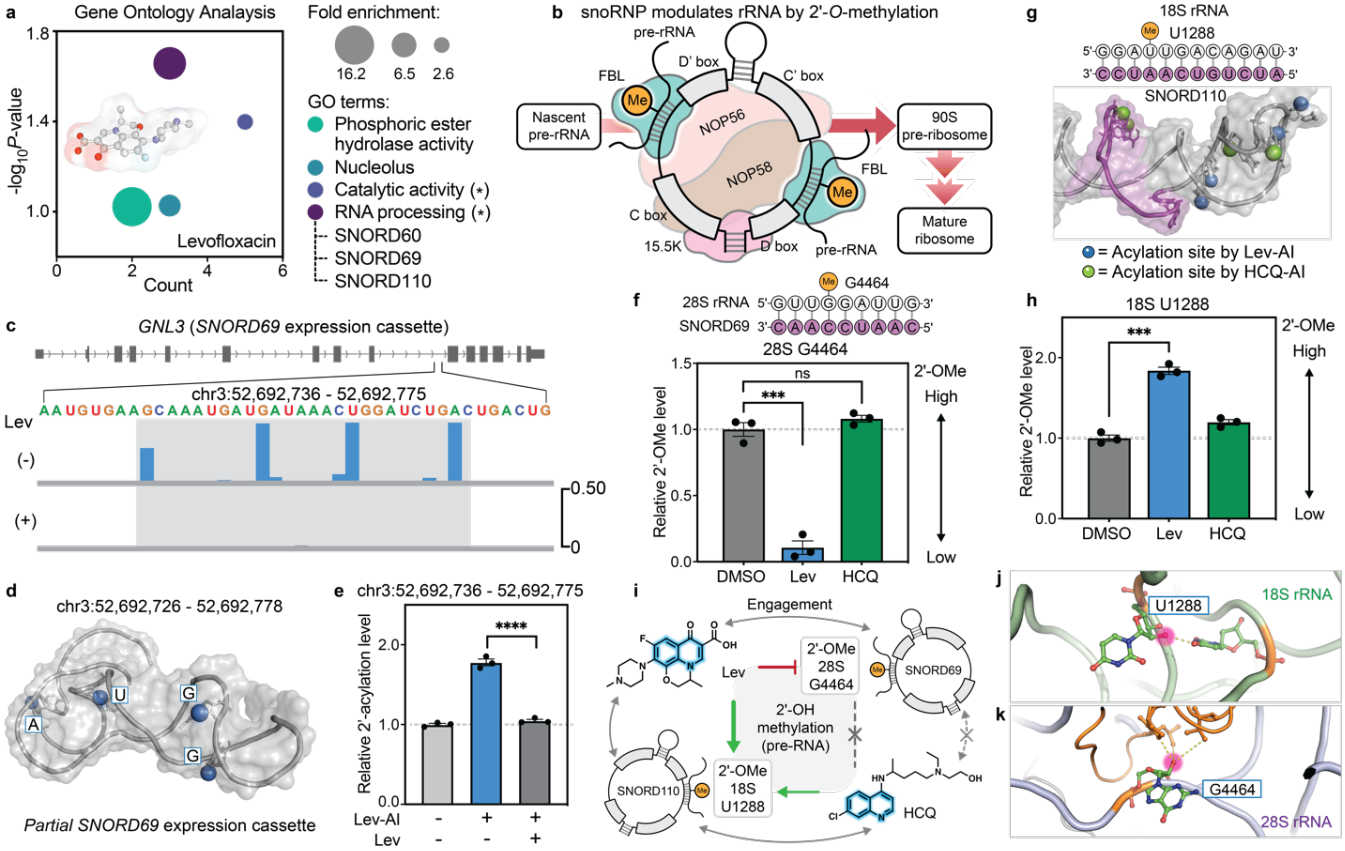

Fig. 4 | RBRP reveals target-associated cellular responses upon drug treatment. **A**, Gene Ontology (GO) analyses of Levofloxacin RNA targets by DAVID tool. GO analysis was performed using DAVID bioinformatics resources 6.8. **b**, Small nucleolar ribonucleoprotein (snoRNP) complex guides 2′-OH methylation of the nascent pre-rRNA. The conserved sequences (box) are annotated. Fibrillarin (FBL), NOP56, NOP58, and 15.5K are small nucleolar proteins. Me indicates the ribosomal 2′-OH to be methylated. **c**, UCSC tracks showing Levofloxacin targets SNORD69 expression cassette of GNL3 pre-mRNA. **d**, Location of drug-promoted 2′-OH acylation by Lev-AI probe mapped onto the RNA model of SNORD69 expression cassette. Acylation sites are labeled as blue spheres. **e**, RT-qPCR validated the relative 2′-acylation level at the indicated sequence of SNORD69 expression cassette. **f**, RT-qPCR showing Levofloxacin reduces 2′-OH methylation of 28S G4464, the methylation target of SNORD69. HCQ does not engage the SNORD69 expression cassette and has no effect on 2′-O-methylation levels of 28S G4464. **g**, Lev-AI and HCQ-AI acylate distinct 2′-OH groups at SNORD110 expression cassette on NOP56 pre-mRNA. SNORD110 mediates 2′-OH methylation of 18S U1288. **h**, Treatment with Levofloxacin, rather than Hydroxychloroquine, enhances 2′-OMe level at 18S U1288. **i**, Schematic comparing the abilities of Levofloxacin and Hydroxychloroquine to modulate 2′-OH methylation of 18S U1288 and 28S G4464. **j-k**, CryoEM structures of the human ribosome showing 2′-OH of 18S U1288 (**j**) and 28S G4464 (**k**) interact with the surrounding rRNA and ribosomal proteins (PDB ID: 4UG0).

AI at this RNA locus—two acylating probes reacted with 2′-OH groups from nearly the opposite sides of the folded SRNOD110 expression sequence (**Fig. 3h**), suggesting distinct binding poses of the two drugs.

RBRP reveals target-associated cellular responses upon drug treatment. To explore possible cellular outcomes of such transcriptome interaction of the three drugs, we performed Gene Ontology (GO) analyses of identified off-target RNAs with Database for Annotation, Visualization and Integrated Discovery (DAVID tool)[35,36]. For example, Levofloxacin binding sites showed significant enrichment for cellular functions associated with biological catalysis and RNA processing (**Fig. 4a**). Three snoRNAs are highly enriched for RNA processing, which can mediate site-specific 2′-OH methylation of nascent pre-rRNA and impact the translational functions of the mature ribosome (**Fig. 4b**)[37,38]. The finding of such RNA off-targets suggests that this drug may potentially influence such a process.

We wondered whether off-target binding of Levofloxacin to the snoRNA expression sequences might affect the ability of mature snoRNAs to methylate their rRNA substrates. To test this, we first investigated how Lev (the unmodified drug) affects the 2′-OH methylation of 28S rRNA:G4464, the methylation substrate of SNORD69[39]. RBRP analysis revealed that Lev engages with a highly structure region within the expression cassette of SNORD69 in HEK293 cells (**Fig. 4c-d**). Using quantitative RT-qPCR, we validated that 2′-OH acylation by Lev-AI probe only occurs in the absence of the competitor drug (unmodified Lev) (**Fig. 4e**). Measurement of ribosome methylation revealed that treatment with Lev potently inhibited the 2′-OH methylation of 28S rRNA:G4464, possibly due to drug-induced conformational changes to the snoRNA and/or disrupted snoRNP formation (**Fig. 4f**). Interestingly, we did not identify any discernible effects on 2′-O-methylation of 28S rRNA:G4464 with HCQ, which interacts at a different site in the snoRNA (**Fig. 4f**). Also notably, RNA off-target interactions of Lev affected snoRNAs beyond SNORD69. Lev also targeted the SNORD110 expression cassette and concurrently enhanced the 2′-O-methylation of its methylation substrate 18S rRNA:U1288 (**Fig. 4h**)[40]. This modulatory effect appears to depend on the binding pose of HCQ versus Lev, as HCQ minimally affected 18S rRNA:U1288 despite targeting the same RNA locus but on the opposite side of folded SNORD110 expression cassette (**Fig. 4h** and **Fig. 3h**). Taken together, our data strongly suggest that

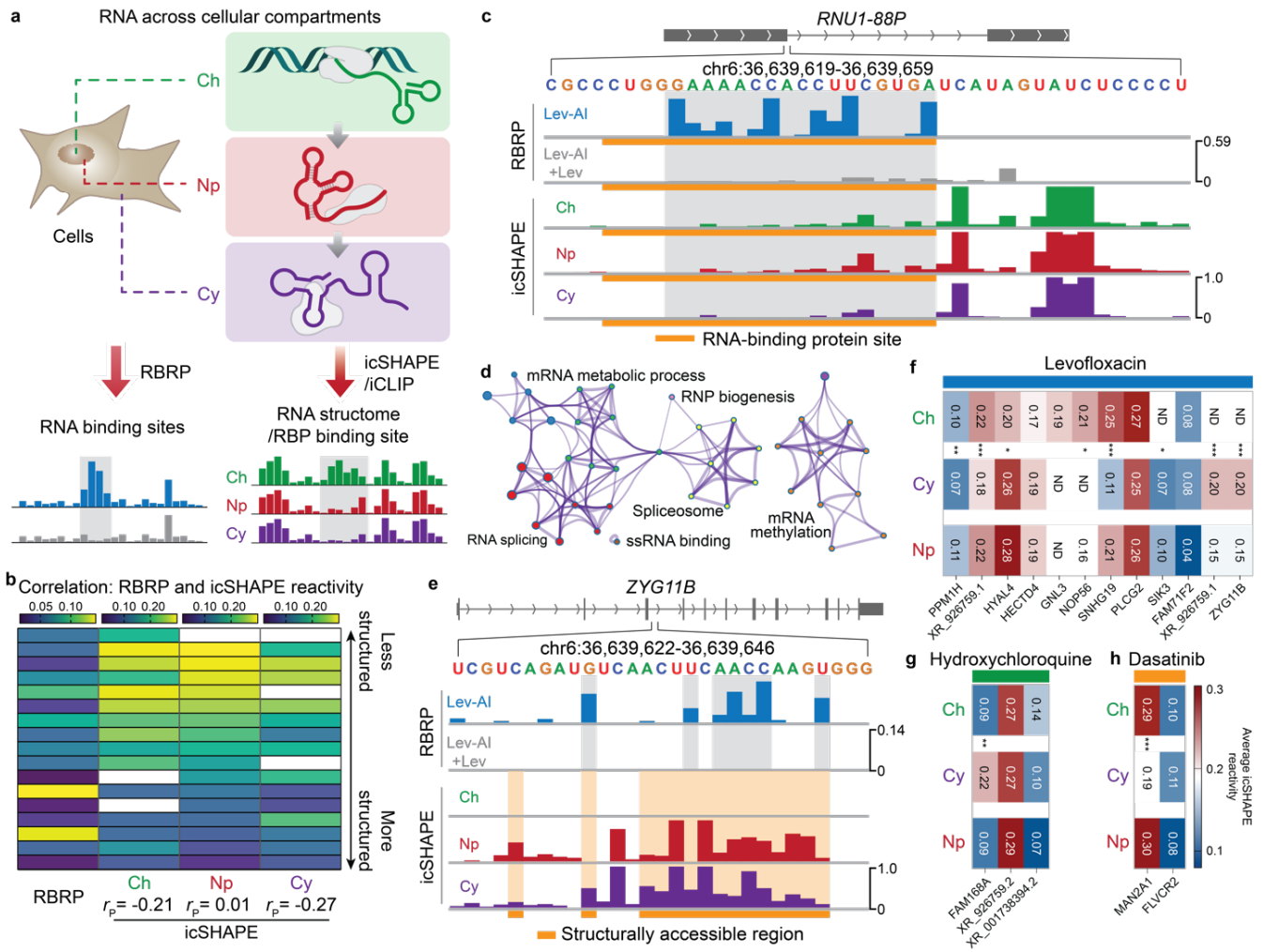

Fig. 5 | Alteration of RNA structure and RBP binding can associate with drug engagement. **a**, Meta-analysis reveals association among RBRP reactivity, RNA structural accessibility, and RBP binding. Ch, chromatin. Np, nucleoplasm. Cy, cytoplasm. **b**, Heatmap showing the Pearson correlation of RBRP and icSHAPE reactivities in three cellular compartments at all identified binding sites. **c**, Lev-AI binds to an RBP-binding site on RNU1-88P RNA. RBP-binding sites were identified using CLIP-seq data from CLIPdb[41]. **d**, Metascape enrichment network showing the top non-redundant enrichment clusters of RNU1-88P-binding proteins at the Lev-AI binding site. **e**, Lev-AI binds to intron 3 of ZYG11B pre-mRNA that has altered structural accessibility in nucleoplasm (Np) compared to cytoplasm (Cy). **f-h**, Heatmap comparing RNA structural accessibility in different cellular compartments at the binding sites of Lev (**f**), HCQ (**g**), and Das (**h**), showing off-target interactions frequently associate with sites of altered structural accessibility across cellular compartments. Values shown are the average icSHAPE reactivities at probe binding sites. *P*-value was calculated using paired t test (**P*<0.05, ***P*<0.01, ****P*<0.001).

FDA-approved protein-targeted drugs can cause unexpected biological outcomes by engaging with their RNA off-targets (**Fig. 4i-k**). Thus, stringent transcriptome-wide validation of drug binding sites should provide more comprehensive insights for the potential mechanism(s) of dose-limiting drug toxicity.

Alteration of RNA structure and RBP binding associates with drug engagement. The ability of RBRP to pinpoint *in vivo* binding sites at each nucleotide of cellular transcripts allows us to assess the roles of RNA structure and RBP in association with their susceptibility to drug binding. We obtained icSHAPE data on *in vivo* transcriptome from previous studies in human HEK293 cells[25,42], and compared icSHAPE reactivity with the tendency of RNA loci to acylation by drug probes (RBRP score) (**Fig. 5a**). We found that the majority, if not all, RNA off-target binding sequences for each tested drug are highly folded and/or RBP-bound *in vivo* (**Fig. 5b**). RBRP and icSHAPE reactivities show minimal correlations in cells, suggesting possible alteration of RNA conformation and/or modulation of RBP interactions upon drug binding that changed the pool of 2′-OH groups accessible for acylation.

RNAs associate extensively with proteins in cells[43]. To infer potential biological effects of RNA off-target binding, we further studied whether a drug may engage with RNA at RBP binding sequences and modulate RBP functions. Taking the off-target U1 small nuclear 88 RNA (RNU1-88P) as an example, we analyzed all of its known RBPs with binding site information from reported cross-linking immunoprecipitation followed by sequencing (CLIP-seq) experiments[41]. RBRP revealed that Lev exclusively engages with a highly structured RBP-binding sequence of RNU1-88P (**Fig. 5c**). The underlying RBPs possess numerous RNA-processing functions (*e.g.*, RNA splicing, m6A methylation) (**Fig. 5d**), suggesting potential perturbation of these RNA functions by Lev. We further extended the analysis to all binding sites of each of the three tested drugs. As shown in **Supplementary file S3**, we found that 42% of off-target binding sites locate at known RBP-binding sequences. These data

allowed us to generate hypotheses to infer biological outcomes of RNA off-target binding.

RNA structure plays a central role in many cellular processes, including RNA transcription, translation, and degradation[25,44,45], and is subject to extensive regulation *in vivo* by RNA modification and RBP interactions that can modulate intermolecular accessibility to structural probing reagents. We observed that RNA off-target binding of the three drugs frequently occurred at sites having structural alterations that vary dynamically between cellular compartments as surveyed recently by icSHAPE[25] (**Fig. 5e-g** and **Supplementary file S4**), suggesting a possible association of drug binding sites with RNA modifications and/or RBP interactions in cells. For example, the folding of ZYG11B locus targeted by the drug Lev varies substantially in the nucleoplasm (Np) relative to the cytoplasm (Cy) (**Fig. 5e**). We applied the same analysis to all identified binding sites of Lev, and found that ~67% of off-target sites are located at RNA loci with altered structural accessibility across cellular compartments (**Fig. 5f-g**). Although we did not find known RNA modifications at these sites, 5 of the 13 off-target sites of Lev are known RBP-binding sites (**Supplementary file S3**). These data suggest widespread interplays between drug binding and RNA-protein interactions in cells, and potential impacts of RNA off-target interactions on biological processes. Thus, the comparative analyses of RBRP, CLIP-seq, and icSHAPE data provide a rich resource to infer biological effects of RNA off-target binding by protein-targeted drugs.

Conclusions

It is generally understood that small-molecule drugs can exhibit toxicity by off-target interactions within the human proteome[46]. Our data suggest that, in addition to proteome interactions, off-target engagement with specific RNAs in the human transcriptome may also be a mechanism by which small molecules cause unintended biological consequences. Each ostensibly protein-targeted drug tested in this study was found to target numerous transcripts in cells. Considering the high chemical similarity of many existing protein-targeted drugs with known RNA-binding molecules (Tanimoto coefficient ≥0.7), this phenomenon is likely common among many FDA-approved drugs and those in clinical trials and preclinical studies. Given that ~90% of drugs fail to receive FDA approval and hundreds of previously approved drugs have been withdrawn[46,47], RNA off targets may likely contribute to failure rates. Stringent characterization of transcriptome interactions for small-molecule drugs may be helpful in shedding light on these problems.

This study highlights the power of reactivity-based RNA profiling (RBRP) for target validation of small-molecule drugs, which requires the use of cell-permeable RNA acylation probes (reacting at 2′-OH groups) and a comparative workflow to scout off-target interactions of drugs in the human transcriptome. RBRP bridges a gap in RNA-sequencing technologies that currently lack the ability to impartially identify drug binding sites at all four nucleotides (**Supplementary Fig. S4**), without potential interference from extended incubation or UV light. The ability to quantify off-target interactions at each nucleotide in more than ~16,000 poly(A)+ RNAs enables unprecedented identification of altered RNA structural accessibility and RBP underlying drug engagement, and allows the users to infer the cellular consequences of off-target RNA binding. Notably, we observed minimal correlation between the RBRP and icSHAPE reactivities transcriptome-wide (**Fig. 5b**), confirming that RBRP signals are drug-promoted rather than simply reflecting structure-dependent stochastic acylation. This observation is also confirmed by the fact that RBRP signals were minimally correlated among three different drugs (**Supplementary Fig. S5**).

Our results indicate that many existing drugs may exert unintended biological effects through off-target interactions with the human transcriptome in cells. For example, we find that off-target transcriptome interaction may unexpectedly affect 2′-OH methylation levels of ribosomal RNAs. Our data show that the antibiotic Lev targets the intronic expression sequence of SNORD69 and causes collateral demethylation of 2′-OMe at 28S rRNA:G4464, the methylation substrate of the mature snoRNP[39]. Not surprisingly, our findings provide evidence that transcriptome interaction of drugs depends greatly on their chemical structures[29,48,49]. Indeed, structural features such as positive charge and flat aromatic structures for groove binding and intercalation can add affinity for structured RNAs *in vitro* with low to moderate selectivity[29,30,50]. Consistently, our work shows that intercalator-like Lev extensively interacts with highly structured RNAs in cells, whereas Das is more structurally complex than a simple intercalator and thus has fewer RNA off targets. Although our work provides strong evidence that transcriptome-interaction can alter cellular outcomes in specific cases, it is likely that some off-target interactions within the human transcriptome will not cause unintended cellular consequences, if the binding does not alter RNA conformation or RPB interactions. In addition, it remains possible that some drug targets will prove to be cell type-dependent, which is not studied here, and will require further investigation.

More broadly, we suggest that rigorous characterization of transcriptome interaction should be essential not only for existing drugs, but also future drugs. Animal toxicity testing fails to predict side-effects and toxicity in ~50% of drugs between Phase I human trials and early post-market withdrawals[51], calling for comprehensive target validation during preclinical studies. Given that dose-limiting toxicity is a chief driver for clinical trial failures and drug withdrawal, stringent validation of drug targets in both the human proteome and transcriptome should not only reduce costs, but also allow the redistribution of resources towards lead compounds that are more likely to pass clinical trials. We envision that RBRP experiments may facilitate our understanding of RNA-mediated drug effects, indicate potential toxicity biomarkers, and characterize toxicity mechanisms.

References

1. Lin, A. *et al.* Off-target toxicity is a common mechanism of action of cancer drugs undergoing clinical trials. *Sci Transl Med* **11** (2019).
2. Onakpoya, I. J., Heneghan, C. J. & Aronson, J. K. Post-marketing withdrawal of 462 medicinal products because of adverse drug reactions: a systematic review of the world literature. *BMC Med* **14**, 10 (2016).
3. Harrison, R. K. Phase II and phase III failures: 2013-2015. *Nat Rev Drug Discov* **15**, 817-818 (2016).
4. Morgan, B. S. *et al.* R-BIND: An Interactive Database for Exploring and Developing RNA-Targeted Chemical Probes. *ACS Chem Biol* **14**, 2691-2700 (2019).
5. Donlic, A. *et al.* R-BIND 2.0: An Updated Database of Bioactive RNA-Targeting Small Molecules and Associated RNA Secondary Structures. *ACS Chem Biol* **17**, 1556-1566 (2022).
6. Kim, S. Exploring Chemical Information in PubChem. *Curr Protoc* **1**, e217 (2021).
7. Suresh, B. M. *et al.* A general fragment-based approach to identify and optimize bioactive ligands targeting RNA. *Proc Natl Acad Sci U S A* **117**, 33197-33203 (2020).

8. Balaratnam, S. *et al.* A chemical probe based on the PreQ1 metabolite enables transcriptome-wide mapping of binding sites. *Nat Commun* **12**, 5856 (2021).
9. Velagapudi, S. P., Li, Y. & Disney, M. D. A cross-linking approach to map small molecule-RNA binding sites in cells. *Bioorg Med Chem Lett* **29**, 1532-1536 (2019).
10. Rzuczek, S. G. *et al.* Precise small-molecule recognition of a toxic CUG RNA repeat expansion. *Nat Chem Biol* **13**, 188-193 (2017).
11. Regulski, E. E. & Breaker, R. R. In-line probing analysis of riboswitches. *Methods Mol Biol* **419**, 53-67 (2008).
12. Zeller, M. J. *et al.* SHAPE-enabled fragment-based ligand discovery for RNA. *Proc Natl Acad Sci U S A* **119**, e2122660119 (2022).
13. Tong, Y. *et al.* Transcriptome-Wide Mapping of Small-Molecule RNA-Binding Sites in Cells Informs an Isoform-Specific Degrader of QSOX1 mRNA. *J Am Chem Soc* (2022).
14. Chang, M. T. *et al.* Identifying transcriptional programs underlying cancer drug response with TraCe-seq. *Nat Biotechnol* **40**, 86-93 (2022).
15. Wurtmann, E. J. & Wolin, S. L. RNA under attack: cellular handling of RNA damage. *Crit Rev Biochem Mol Biol* **44**, 34-49 (2009).
16. Ravanat, J. L., Douki, T. & Cadet, J. Direct and indirect effects of UV radiation on DNA and its components. *J Photochem Photobiol B* **63**, 88-102 (2001).
17. Qiu, Z., Lu, L., Jian, X. & He, C. A diazirine-based nucleoside analogue for efficient DNA interstrand photocross-linking. *J Am Chem Soc* **130**, 14398-14399 (2008).
18. Nakamoto, K. & Ueno, Y. Diazirine-containing RNA photo-cross-linking probes for capturing microRNA targets. *J Org Chem* **79**, 2463-2472 (2014).
19. Di Antonio, M., McLuckie, K. I. & Balasubramanian, S. Reprogramming the mechanism of action of chlorambucil by coupling to a G-quadruplex ligand. *J Am Chem Soc* **136**, 5860-5863 (2014).
20. Spitale, R. C. *et al.* Structural imprints in vivo decode RNA regulatory mechanisms. *Nature* **519**, 486-490 (2015).
21. Shahsavarinia, K. *et al.* An Umbrella Review of Clinical Efficacy and Adverse Cardiac Events Associated with Hydroxychloroquine or Chloroquine with or Without Azithromycin in Patients with COVID-19. *Anesth Pain Med* **11**, e115827 (2021).
22. Begley, C. G. *et al.* Drug repurposing: Misconceptions, challenges, and opportunities for academic researchers. *Sci Transl Med* **13**, eabd5524 (2021).
23. Flynn, R. A. *et al.* Transcriptome-wide interrogation of RNA secondary structure in living cells with icSHAPE. *Nat Protoc* **11**, 273-290 (2016).
24. Corsello, S. M. *et al.* The Drug Repurposing Hub: a next-generation drug library and information resource. *Nat Med* **23**, 405-408 (2017).
25. Sun, L. *et al.* RNA structure maps across mammalian cellular compartments. *Nat Struct Mol Biol* **26**, 322-330 (2019).
26. Marchant, J. When antibiotics turn toxic. *Nature* **555**, 431-433 (2018).
27. Force, T. & Kolaja, K. L. Cardiotoxicity of kinase inhibitors: the prediction and translation of preclinical models to clinical outcomes. *Nat Rev Drug Discov* **10**, 111-126 (2011).
28. Backman, T. W., Cao, Y. & Girke, T. ChemMine tools: an online service for analyzing and clustering small molecules. *Nucleic Acids Res* **39**, W486-491 (2011).
29. Padroni, G., Patwardhan, N. N., Schapira, M. & Hargrove, A. E. Systematic analysis of the interactions driving small molecule-RNA recognition. *RSC Med Chem* **11**, 802-813 (2020).
30. Guo, P. *et al.* Compound Shape Effects in Minor Groove Binding Affinity and Specificity for Mixed Sequence DNA. *J Am Chem Soc* **140**, 14761-14769 (2018).
31. Rigau, M., Juan, D., Valencia, A. & Rico, D. Intronic CNVs and gene expression variation in human populations. *PLoS Genet* **15**, e1007902 (2019).
32. Stoll, L. *et al.* A circular RNA generated from an intron of the insulin gene controls insulin secretion. *Nat Commun* **11**, 5611 (2020).
33. Rearick, D. *et al.* Critical association of ncRNA with introns. *Nucleic Acids Res* **39**, 2357-2366 (2011).
34. Pan, Q., Shai, O., Lee, L. J., Frey, B. J. & Blencowe, B. J. Deep surveying of alternative splicing complexity in the human transcriptome by high-throughput sequencing. *Nat Genet* **40**, 1413-1415 (2008).
35. Sherman, B. T. *et al.* DAVID: a web server for functional enrichment analysis and functional annotation of gene lists (2021 update). *Nucleic Acids Res* (2022).
36. Huang da, W., Sherman, B. T. & Lempicki, R. A. Systematic and integrative analysis of large gene lists using DAVID bioinformatics resources. *Nat Protoc* **4**, 44-57 (2009).
37. Khoshnevis, S., Dreggors-Walker, R. E., Marchand, V., Motorin, Y. & Ghalei, H. Ribosomal RNA 2'-O-methylations regulate translation by impacting ribosome dynamics. *Proc Natl Acad Sci U S A* **119**, e2117334119 (2022).
38. Jansson, M. D. *et al.* Regulation of translation by site-specific ribosomal RNA methylation. *Nat Struct Mol Biol* **28**, 889-899 (2021).
39. Deryusheva, S., Talhouarne, G. J. S. & Gall, J. G. "Lost and Found": snoRNA Annotation in the Xenopus Genome and Implications for Evolutionary Studies. *Mol Biol Evol* **37**, 149-166 (2020).
40. Krishnan, P. *et al.* Profiling of Small Nucleolar RNAs by Next Generation Sequencing: Potential New Players for Breast Cancer Prognosis. *PLoS One* **11**, e0162622 (2016).
41. Yang, Y. C. *et al.* CLIPdb: a CLIP-seq database for protein-RNA interactions. *BMC Genomics* **16**, 51 (2015).
42. Lu, Z. *et al.* RNA Duplex Map in Living Cells Reveals Higher-Order Transcriptome Structure. *Cell* **165**, 1267-1279 (2016).
43. Van Nostrand, E. L. *et al.* A large-scale binding and functional map of human RNA-binding proteins. *Nature* **583**, 711-719 (2020).
44. Mustoe, A. M. *et al.* Pervasive Regulatory Functions of mRNA Structure Revealed by High-Resolution SHAPE Probing. *Cell* **173**, 181-195 e118 (2018).
45. Mortimer, S. A., Kidwell, M. A. & Doudna, J. A. Insights into RNA structure and function from genome-wide studies. *Nat Rev Genet* **15**, 469-479 (2014).
46. Pottel, J. *et al.* The activities of drug inactive ingredients on biological targets. *Science* **369**, 403-413 (2020).
47. Mullard, A. Parsing clinical success rates. *Nat Rev Drug Discov* **15**, 447 (2016).
48. Morgan, B. S., Forte, J. E., Culver, R. N., Zhang, Y. & Hargrove, A. E. Discovery of Key Physicochemical, Structural, and Spatial Properties of RNA-Targeted Bioactive Ligands. *Angew Chem Int Ed Engl* **56**, 13498-13502 (2017).
49. Cai, Z., Zafferani, M., Akande, O. M. & Hargrove, A. E. Quantitative Structure-Activity Relationship (QSAR) Study Predicts Small-Molecule Binding to RNA Structure. *J Med Chem* **65**, 7262-7277 (2022).
50. Vicens, Q. & Westhof, E. RNA as a drug target: the case of aminoglycosides. *Chembiochem* **4**, 1018-1023 (2003).
51. Van Norman, G. A. Limitations of Animal Studies for Predicting Toxicity in Clinical Trials: Is it Time to Rethink Our Current Approach? *JACC Basic Transl Sci* **4**, 845-854 (2019).
52. Dong, Z. W. *et al.* RTL-P: a sensitive approach for detecting sites of 2'-O-methylation in RNA molecules. *Nucleic Acids Res* **40**, e157 (2012).

Methods

Materials. DNA and RNA were purchased from IDT or Stanford PAN facility unless otherwise stated (see **Supplementary Table S4** for details). All chemicals purchased from commercial suppliers were used without further purification (see **Supplementary Table S5** for details). All enzymes, kits, bioreagents, and software were obtained from sources listed in Supplementary Table S5. Human cell line HEK293 (CRL-1573) was purchased from American Type Culture Collection (ATCC) and maintained in DMEM supplementary with 10% fetal bovine serum at 37 ˚C in a humidified incubator containing 5% CO_2.

Synthesis of acylimidazole probes. HCQ-AI, Lev-AI, and Das-AI were synthesized as described in the Supplementary Information and activated immediately before use: In general, the carboxylic acid precursors (1.0 equiv.) were dissolved in dry DMSO. To it was added a suspension containing 1.3 equivalent of 1,1'-carbonyldiimidazole (CDI) at room temperature. The solution was stirred at room temperature overnight under argon. After the reaction, the final solution can be used as a 50 mM acylimidazole stock without further purification. See Supplementary Information for details.

Curation of small-molecule drugs database. Database curation of FDA-approved drugs. Lists of FDA-approved small-molecule drugs were acquired from a previous study[5]. Briefly, FDA-approved drugs were downloaded from DrugBank (v5.1.6, released on 04/22/2020. ref) on 06/15/2020. The drug list was further filtered to remove molecules according to the reported criteria[5]. Molecules with molecular weights larger than 140 Da and smaller than 706 Da were used for statistical and principal components analysis.

Database curation of drugs in preclinical studies, clinical trials, and drugs withdrawn from the market. The small molecules were acquired from Drug Repurposing Hub[24] on 06/05/2022. The molecules were annotated based on their disease areas and stages in clinical studies. Molecules with molecular weights that are larger than 140 Da and smaller than 706 Da were used for statistical analysis.

Database curation of RNA-binding small-molecule ligands (RNA binders). The small-molecule (SM) RNA binders were downloaded from R-bind 2.0[5] on 05/24/2022. Molecules (131) with known PubChem Compound ID number (CID) were further used for Structural similarity analysis using the Tanimoto coefficient (Tc).

Quantification of structural similarity with Tanimoto coefficient (Tc). Substructure key-based 2D Tanimoto coefficients were calculated using PubChem Score Matrix Service. Lists of CIDs for 131 known RNA binders and molecules of interest were used as input to calculate the pairwise Tanimoto coefficients with each of 131 known RNA binders. Tanimoto coefficients of all drug-RNA binder pairs are listed as the matrix in **Supplementary file S1**.

Chemoinformatic calculation of chemical fingerprints. Fourteen Open Babel descriptors of the selected FDA-approved drugs were calculated using ChemMine Tools[28]. See **Supplementary file S2** for the detailed list.

Principal component analysis of chemical fingerprints of small-molecule drugs. Fourteen Open Babel descriptors were used as chemical fingerprints in the standardized principal component analysis (PCA). PCA was performed using Graphpad Prism 9. The principal components (PC1 and PC2) were selected based on parallel analysis, with eigenvalues greater than 95% percentile of Monte Carlo simulations (number of simulations: 1,000) on "random" data of equal dimension to the input data. See **Supplementary Tables S1-2** for details.

Treatment of cells with acylimidazole probes, isolation of total cellular RNA, and enrichment of poly(A)+ transcripts. ~$2x10^6$ of cells were pretreated with DMSO or excess competing drugs for 30 minutes at 37 ˚C. The cells were then immediately scraped into a 15-mL falcon tube and resuspended in 1 mL of 1xPBS, pH=7.4 at 37 ˚C containing 50 μM of acylimidazole probe, in the absence or presence of excess competing drugs. After incubation at 37 ˚C for 30 minutes, the reaction was stopped by centrifugation. See Supplementary Information for details.

To isolate total cellular RNA, cells were lysed with 6 mL of Trizol LS reagent according to the Supplementary Information. RNAs were then purified with a Zymo Quick-RNA Midiprep kit according to the manufacturer's protocol.

To enrich poly(A)+ transcripts, a 250-μg aliquot of total cellular RNA was diluted to 600 μg/mL with RNA storage buffer and then purified with Poly(A)Purist MAG kit according to the manufacturer's protocol. The captured RNAs were further purified with RNeasy Mini columns according to the manufacturer's protocol, and stored as 500-ng aliquots at -80 ˚C.

Preparation of sequencing libraries. Sequencing libraries were prepared according to the following protocol based on a previous report[20,23] with modifications: First, the probe-labeled RNAs were modified with biotin by "click" reaction. 500 ng of poly(A)+ RNAs were incubated with 2 μL of 1.85 mM DIBO-Biotin and 1 μL of RiboLock at 37 ˚C for 2 hours. After the reaction, modified RNAs were purified with a Zymo RNA Clean & Concentrator column-5 according to the manufacturer's protocol.

(RNA fragmentation, 3′-end repair, and 3′-end ligation) RNAs were fragmented using RNA fragmentation reagent, with rendered RNA fragments with a medium length ~100 nt. After purification with a Zymo RNA Clean & Concentrator column-5, the 3′-end of RNA fragments were repaired by FastAP and T4 PNK for 1 hour at 37 ˚C according to the previously reported protocol[20,23]. Next, 3′-ligation was performed to install an 3′-blocked RNA ligand to the 3′-end of RNA fragments. Briefly, RNAs were incubated with T4 RNA ligase 1 and preadenylylated RNA links (Probe-treated sample: 3′-ddC blocked RNA linker /5rApp/AGA TCG GAA GAG CGG TTC AG/3ddC/ was used; For DMSO-treated samples, 3′-biotin blocked RNA linker /5rApp/AGA TCG GAA GAG CGG TTC AG/3Biotin/ was used. After the 3′-end ligation reaction, RNA was purified with a Zymo RNA Clean & Concentrator Column-5 and then resolved on a 6% (w/v) UreaGel denaturing PAGE. RNAs with a length above ~50 nt were extracted and further purified using a 10K Amicon filter as described in Supplementary Information.

(cDNA synthesis, enrichment of Biotin-modified RNAs, and cDNA purification) The following steps were performed according to the previously reported protocol with slight modifications[20,23]: The 3′-ligated RNA was dissolved in 11 μL of RNase-free water and 1 μL of 1 μM barcoded RT primer (/5phos/DDD NNA ACC NNN NAG ATC GGA AGA GCG TCG TGG A/iSp18/GGATCC/iSp18/TACTGAACCGC. D = A/G/T and N = A/T/G/C. The underlined four nucleotides are barcodes)(see Supplementary Table S4 for assignments of RT primers). The reaction was heated at 70 ˚C for 5 minutes and then

cooled to 25 ˚C by 20˚C/60 seconds. 8 μL of RT reaction mixture (4 μL of 5x First strand buffer, 0.75 μL of RiboLock, 1 μL of 100 mM DTT, 1 μL of 10 mM dNTPs, and 1.25 μL of SuperScript III) was then added to the above reaction. The resulting solution was heated at 25 ˚C for 3 mins, 42 ˚C for 5 mins, and 52 ˚C for 30 mins. Next, the cDNA-RNA heteroduplexes were enriched with MyOne C1 magnetic streptavidin beads and the cDNA was purified with a 6% (w/v) denaturing PAGE gel as described in the Supplementary Information.

(cDNA circularization and library amplification) The purified cDNA was circularized with CircLigase II for 3 hours at 60 ˚C and purified with Zymo DNA Clean & Concentrator Column-5 according to the manufacturers' protocols. To amplify the library, 20 μL of 2x Phusion HF PCR master mix, 0.4 μL of SYBR Green I (25x), 1.0 μL of 10 μM P5-universal PCR primer (5′-AAT GAT ACG GCG ACC ACC GAG ATC TAC ACT CTT TCC CTA CAC GAC GCT CTT CCG ATC T-3′ and 10 μM P3-universal PCR primer (5′-CAA GCA GAA GAC GGC ATA CGA GAT CGG TCT CGG CAT TCC TGC TGA ACC GCT CTT CCG ATC T-3′). PCR amplification was monitored in real-time to avoid over-amplification. The PCR reaction was first denatured at 98 ˚C for 45 seconds, followed by cycles of denaturation (98 ˚C, 15 seconds), Anneal (65 ˚C, 20 seconds), and Extension (72 ˚C, 1 minute). The PCR products were purified with a 3% low melting point agarose gel and extracted with the QIAGEN MiniElute Gel extraction kit. The purified DNA was analyzed by BioAnalyzer for quality control and quantified with Qubit.

Next-generation sequencing. Ten sub-libraries were combined as a sequence library. The sequence library was sequenced on an Illumina-based HiSeq X-ten with a 23% spike-in PhiX sequencing control. Paired-end 150 bp sequencing was performed. The raw data were transformed into single-end reads for the following bioinformatics analysis with the icSHAPE pipeline. Note: the DMSO-treated sequence sub-libraries are amplified for fewer cycle numbers and thus have higher complexity than the probe-treated sequence sub-libraries. Thus, more sequencing depth should be allocated to the probe-treated sequence sub-libraries.

Bioinformatics and RBRP data visualization. We use a bioinformatics pipeline modified based on icSHAPE[20,23] to calculate the averaged frequency of reverse transcription stops as the RBRP reactivity at each nucleotide transcriptome wide. See Supplementary Information for detailed protocols and command lines. Bigwig files can be visualized using alignment visualization tools such as Integrative Genomics Viewer (IGV) or UCSC Genome Browser.

Identification of off-target RNA binding sites. RBRP acylation sites that can be competed by the competing drug were visually inspected. The average RBRP reactivity of a 100 nt-window covering the competed acylation sites was calculated (see **Supplementary file S4** for all competed acylation sites). The enrichment score for each cluster of acylation sites was calculated as the ratio of relative RBRP reactivity for experiments in the absence over the presence of excess competing drugs. One-tailed t-test was performed to calculate the P-value using the enrichment scores for each replicate in the absence and presence of excess competing drugs. We defined potential RNA-binding sites as nucleotides with enrichment scores ≥3 and P-values <0.05.

Validation of probe-promoted acylation by RT-qPCR. 500 ng (10 μL, 50 ng/μL) of polyA(+) RNA from DMSO-treated libraries or probe-treated libraries in the absence or presence of excess competing drugs were mixed with 1 μL of 10 mM dNTPs, 2 μM RT primer (see **Supplementary Table S4**), and 1 mL of water. The reaction mixture was heated at 65 ˚C for 5 minutes and then cooled on ice for > 1 minute. Next, 4 μL of 5x first-strand buffer, 1 μL of 0.1 M DTT, 1 μL of RiboLock, and 1 μL of SuperScript III was added to the reaction. The reaction solution was then incubated at 55 ˚C for 50 minutes, followed by incubation at 70 ˚C for 15 minutes.

To quantify cDNA, 2 μL of the above cDNA product was added to a solution containing 1.25 μL of 10 μM forward primer (upstream: U), 1.25 μL of 10 μM reverse primer, 12.5 μL 2x Phusion HF master mix, 0.75 μL of 8.33x SYBR Green I, and 7.25 μL of water. Separately, we set up a loading control experiment. 2 μL of the above cDNA product was added to a solution containing 1.25 μL of 10 μM forward primer (downstream: D), 1.25 μL of 10 μM reverse primer, 12.5 μL 2x Phusion HF master mix, 0.75 μL of 8.33x SYBR Green I, and 7.25 μL of water. The resulting mixture was amplified using a StepOnePlus real-time qPCR system, starting with an initial denaturation step at 98 ˚C for 45 seconds, followed by 40 cycles of denaturation (98 ˚C, 15 seconds), anneal (65 ˚C, 20 seconds), and extension (72 ˚C, 60 seconds). ΔCt value was calculated by subtracting Ct(U) by Ct(D): ΔCt=Ct(U)-Ct(D). An increased ΔCt value indicates acylation at the tested sites.

RNA modeling with icSHAPE data. *In vivo* RNA structural probing data was acquired from a prior study[25] to characterize the structure of off-target RNA binding sites. RNA sequences that cover the acylation sites and icSHAPE-determined RNA accessibility were input into RNAComposer, which generates three-dimensionally folded RNA. The structure file was then visualized and processed by PyMOL.

Quantification of the 2′-O-methylation level of human rRNA. To quantify 2′-O-methylation of rRNA, we performed Reverse Transcription at Low deoxy-ribonucleoside triphosphate (dNTP) concentrations followed by polymerase chain reaction (PCR) (RTL-P)[52]. Briefly, RTL-P measures relative 2′-O-methylation by comparing qPCR efficiency after reverse transcription in low (0.5 μM) and normal (0.5 mM) dNTP concentrations. RT is inhibited at 2′-O-methylation sites at low dNTP concentration (0.5 μM), but not at standard dNTP concentration (0.5 mM). The efficiency of RT reaction can be quantified by qPCR, which will be normalized to an internal control where a set of primers quantify rRNA at sites 3′- of the acylation sites. We expect increased RT efficiency with loss of 2′-O-methylation.

To determine how treatment with Hydroxychloroquine or Levofloxacin affects 2′-O-methylation of rRNA, we first plated HEK293 cells on a 6-well plate in 2 mL DMEM containing 10% FBS. 20 μL of DMSO or concentrated DMSO solution of HCQ or Lev were then added to the cells to reach drug concentrations at 0 μM, 50 μM, 25 μM, 13 μM, 6.3 μM, or 3.2 μM. The cells were incubated at 37 ˚C in a humidified incubator containing 5% CO2 for two days. After two days, cells were washed with 2 mL of DPBS and then lysed with 600 μL of Trizol LS reagent, followed by RNA purification with Quick RNA-miniprep kits and on-column digestion of genomic DNA. The concentration of eluted RNA was estimated by Nanodrop and normalized to 100 ng/μL with RNase-free water.

For RTL-P, reverse transcription was performed with 500 ng extracted RNA (5 μL), 1 μL of 10 μM (low) or 10 mM (high) dNTP, 1 μL of 2 μM RT primer. The solution was heated at 65 ˚C for 5 minutes and then incubated on ice for > 1 minute. Next, 4 μL of 5x First-strand buffer, 1 μL of 0.1 M DTT, 1 μL of RiboLock, and 1 μL of SuperScript III were added to the reaction. The reaction mixture was then incubated at 55 ˚C for 50 minutes, followed by incubation at 70 ˚C for 15 minutes.

Two separate sets of qPCR experiments were performed for each RT reaction. In one experiment, 2 μL of cDNA product was mixed with 1.25 μL of 10 μM forward primer (upstream: U) and 1.25 μL of 10 μM reverse primer, 12.5 μL of 2x Phusion HF Master mix, 0.75 μL of 8.33x SYBR Green I, and 7.25 μL water. In a separate reaction, 2 μL of cDNA product was mixed with 1.25 μL of 10 μM forward primer (downstream: D) and 1.25 μL of 10 μM reverse primer, 12.5 μL of 2x Phusion HF Master mix, 0.75 μL of 8.33x SYBR Green I, and 7.25 μL water. This reaction serves as an internal control that quantifies the relative amount of rRNA. The resulting mixture was amplified using a StepOnePlus real-time qPCR system starting with an initial denaturation at 98 ˚C for 45 seconds, followed by 40 cycles of denaturation (98 ˚C, 15 seconds), anneal (65 ˚C, 20 seconds), and extension (72 ˚C, 60 seconds). ΔCt value was calculated by subtracting Ct(U) by Ct(D): ΔCt=Ct(U)-Ct(D). An increased ΔCt value indicates loss of 2′-O-methylation at the targeted sites.

Statistical analysis. For all statistical tests (unless otherwise noted), an one-tailed or two-tailed Student's t-test was used to compare means between two samples. Significance is denoted as follows: * = $P< 0.05$, ** = $P< 0.01$, *** = $P< 0.001$, **** = $P< 0.0001$. Student's t-tests were performed in GraphPad Prism9 software. Pearson correlation was used to quantify pairwise correlation of RBRP reactivities between RBRP libraries transcriptome wide. Pearson correlation was calculated by WiggleTools 1.2. Quantifications shown are mean ± s.e.m. unless otherwise stated.

Data availability

Data supporting the findings of this study are available in the article, Supplementary Information, and Supplementary files S1-S4. Source data and all downloadable bigwig files containing the RBRP reactivities are also available at Figshare at https://doi.org/10.6084/m9.figshare.20326824.

Acknowledgements

We acknowledge support from U.S. National Institutes of Health (GM130704 and GM145357) for support of this work. We thank Dr. Anita Đonlić and Emily G. Swanson for sharing the list of FDA-approved drugs. We thank staffs at Stanford PAN facility for supports with oligo synthesis.

Competing interests

The authors declare no competing financial interests.